Short Communication

Preparation and Properties of Bismuth Molybdate (Bi₂MoO₆) as Photoanode for Methylene Blue Degradation

Juanqin Xue[1], Fei Li[1], Shuhao Li[2], Jian Zhang[1], Qiang Bi[1,]*

[1] School of Chemistry and Chemical Engineering, Xi'an University of Architecture and Technology, Xi'an 710055, Shaanxi, China
[2] School of Metallurgical Engineering, Xi'an University of Architecture and Technology, Xi'an 710055, Shaanxi, China
*E-mail: Bxqiang12@126.com

Bismuth molybdate (Bi₂MoO₆) is a promising visible-light-responsive material that can be used as a photoanode for photoelectrocatalytic oxidation. In order to enhance the photoelectrocatalytic performance of bismuth molybdate as a photoanode, this paper controlled its morphology by surfactants and investigated the relationship between its morphology and property. The base material was prepared by hydrothermal method with cetyltrimethylammonium bromide (CTAB) as surfactant, and the powder was subjected to continuous dip coating to form a nanosheet Bi₂MoO₆ photoanode. The morphology of Bi₂MoO₆ prepared by adding surfactant turned from granular shape to smaller and thinner nanosheet structure, and the band gap of Bi₂MoO₆ photoelectrode changed from 2.57 eV to 2.23 eV, with a photocurrent of around 0.029 μA/cm², which was 1.5 times stronger than that of the Bi₂MoO₆ photoelectrode obtained without adding surfactant. Additionally, the photoelectrode degradation efficiency of methylene blue increased by 26%. The results indicated that the Bi₂MoO₆ powder obtained under the experimental conditions exhibited better photocatalytic performance. Therefore, this paper will provide theoretical basis and technical support for preparing high-performance photocatalytic materials.

1. INTRODUCTION

Azo dyes are the main pollutants in the waste water produced by textile, paper, printing and leather industries. Such kind of waste water is carcinogenic, teratogenic, mutagenic and harmful to human health and ecological environment. Azo pollutants are strongly toxic and can severely inhibit the growth of microorganisms, so traditional biochemical treatment is no longer effective, and effective

methods of treating such waste water need to be urgently developed. A variety of advanced oxidation techniques have been applied to treat such waste water [1-3]. Unfortunately, some of these techniques require some demanding conditions such as high temperature, high pressure or expensive precious metal catalysts. Photocatalytic technology is considered to be an effective method for treating such waste water due to its advantages of high efficiency, low consumption, extensive application and environmental friendliness [4,5]. However, TiO_2, "the first-generation photocatalytic material", is only responsive to ultraviolet light, which only accounts for approximately 5% of the sunlight. Therefore, the development of new materials that are highly responsive to visible light is of great significance for the practical application of photoelectrocatalysis technology.

In recent years, new non-titanium-based visible light-driven catalytic materials such as Bi_2MoO_6[6,7], $InVO_4$[8], and $AgAlO_2$[9,10] have become increasingly popular due to their strong response to visible light. Compared with TiO_2, Bi_2MoO_6 can absorb visible light and exhibit superior performance, so its potential application value has attracted widespread attention. However, there are two major obstacles to the photocatalytic degradation of pollutants by Bi_2MoO_6. One is its poor oxidation kinetics in water, and the other is the rapid recombination between photoelectrons and holes, which is why the application of Bi_2MoO_6 is somewhat limited.

The easy recombination between photoelectrons and holes can be prevented by utilizing Bi_2MoO_6 as a photoelectrode and applying bias voltage. The water oxidation kinetics of Bi_2MoO_6 are mainly affected by the microstructure of its active sites, its specific surface area and morphology. And the photocatalytic degradation of Bi_2MoO_6 can be effectively enhanced by regulating its morphology[15,16]. In this study, surfactants were used to control the morphology of Bi_2MoO_6, which changed from an irregular granular shape to a regular nanosheet structure, thus improving the water oxidation kinetics of Bi_2MoO_6 and increasing its catalytic sites because nanosheet structure could provide a high specific surface area[17-19]. Meanwhile, the band gap of Bi_2MoO_6 was reduced while its carrier density was increased, thus enhancing its catalytic activity. Additionally, a thin-film photoanode was prepared by continuous dip coating, which would be used for treating dye waste water. The experimental results indicated that the photoelectrocatalytic performance and water oxidation kinetics of Bi_2MoO_6 were greatly improved. Therefore, this paper will provide theoretical basis and technical support for preparing high-performance photocatalytic materials.

2. EXPERIMENTAL

2.1 Bi_2MoO_6 Photocatalyst

Nanosheet Bi_2MoO_6 was prepared by hydrothermal method. Typically, $Na_2MoO_4 \cdot 2H_2O$ and $Bi(NO_3)_3 \cdot 5H_2O$ were mixed in a molar ratio of 1:2 for synthesizing Bi_2MoO_6, and then the surfactant CTAB was added and dissolved, thus changing the molar ratio of CTAB, $Na_2MoO_4 \cdot 2H_2O$ and $Bi(NO_3)_3 \cdot 5H_2O$ to be 2:5:10. Finally, the mixed solution was transferred to a 100 mL polytetrafluoroethylene reactor for reaction at a temperature of 120°C for 24 h. After reaction was over, the product was cooled to room temperature, washed continuously with deionized water and absolute

ethanol, and dried at 60°C for constant mass.

The growth mechanism ofBi_2MoO_6 nanosheet is shown in Figure 1. As can be seen from the figure, CTA^+ (a cation with a hydrophobic group, the cationic of CTAB dissociated in water) electrostatically and sterically reacted with $MoO4^{2-}$ in the solution, thus reducing the nucleation rate of Bi_2MoO_6 particles and further effectively controlling its growth and morphology. Subsequently, Bi_2MoO_6 particles were continuously aggregated, gradually growing into a thinner and smaller nanosheet structure because its (anisotropic) characteristics altered.
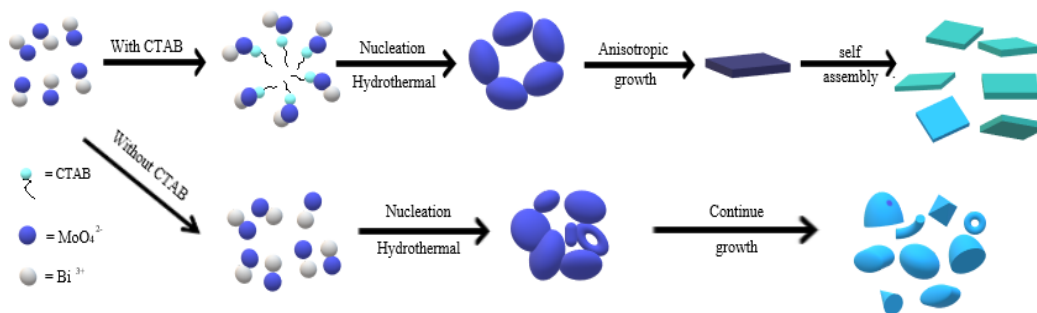

Figure 1. Growth mechanism of Bi_2MoO_6 nanosheet

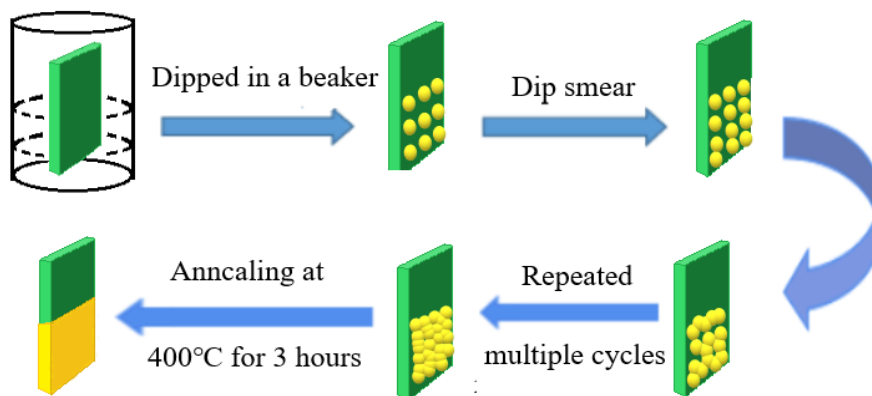*2.2 Preparation of Bi_2MoO_6 photoanode*

Figure 2. Growth process of Bi_2MoO_6 nanosheet photoanode

The growth process of Bi_2MoO_6 nanosheet photoanode is shown in Figure 2. The nanosheet Bi_2MoO_6 and polyethylene glycol 400 were ground in an agate mortar with a mass ratio of 5:1, and then a small amount of anhydrous ethanol was added for dip coating. Firstly, F-doped SnO_2 was obtained. The conductive substrate (FTO, 1.6 mm thick, surface resistance of 15 ohm/sq) was impregnated with the precursor solution, and then placed with its conductive side facing up and taped (Scotch, 50 μm thick) to the four sides of conductive glass. Secondly, Bi_2MoO_6 was formed on the conductive glass by dip coating absorption, and a multilayer precursor was prepared by repeating the above process for several times and then dried at a temperature of 60°C. Finally, the Bi_2MoO_6

photoelectrode was obtained by annealing at 400°C for 3 h in a muffle furnace. The samples with and without adding surfactant CTAB were then labeled as BMO-0 and BMO-1, respectively.

2.3 Characterization methods

The morphology of the Bi_2MoO_6 photoanode was observed by field emission scanning electron microscopy (FESEM) (JSM-7500F), and the crystal structure of the sample was measured using a D8AA25 type X-ray diffractometer (XRD). The UV-visible light absorption study was carried out by photographing the diffuse reflectance spectrum (DRS) of the photoanode using a UV-Vis NIR spectrophotometer (PerkinElmer, Lambda 750S) equipped with an integrated sphere 60 mm in diameter. The structure of the material was characterized by Raman spectroscopy.

2.4 Evaluation of visible-light catalytic activity

The visible-light catalytic activity of the Bi_2MoO_6 photoelectrode was investigated in a glass reactor with a 300 W xenon lamp as the source of visible light and 10 mg/L methylene blue as the target of degradation. The specific steps were as follows: Firstly, the Bi_2MoO_6 photoelectrode was placed in the solution of methylene blue in a dark box for 30 min to achieve adsorption/desorption equilibrium. Secondly, the reactor was placed in the light 12 cm away from the light source and magnetically stirred for further reaction for 180 min. Finally, the absorbance of methylene blue of the Bi_2MoO_6 photoanode was tested by UV-2450 UV-Vis spectrophotometer at a wavelength of 664 nm. One sample was selected every 30 min. And the concentration of the solution was calculated from its absorbance according to Lambert-Beer's law. The degradation rate of methylene blue can be calculated by the following formula:

$$\eta=(C_0-C)/C_0\times100\%=(A_0-A)/A_0\times100\% \tag{1}$$

where C_0 is the initial concentration of methylene blue, C is the concentration of methylene blue after photoelectrocatalytic oxidation for a certain period of time, A_0 is the initial absorbance of methylene blue, and A is the absorbance of methylene blue after photoelectrocatalytic oxidation for a certain period of time.

2.5 Evaluation of photoelectrochemical performance

The photoelectrochemical properties of the prepared samples were tested by using a three electrode system combined with simulated sunlight front irradiation. The sample electrode with an area of 1 cm2 was selected as the working electrode, Pt electrode as the counter electrode and Ag/AgCl (saturated KCl) as the reference electrode. The simulated sunlight is obtained by a 300W xenon lamp (NBet HSX-F300, China) equipped with AM 1.5G filter. Using electrochemical workstation (CORRTEST, China), with 0.5 mol/L Na2SO4 buffer as electrolyte, electrochemical impedance spectroscopy (EIS) data was measured at a sinusoidal voltage disturbance voltage of 10mV between 100 kHz and 0.1 Hz, and measured at Scan from -0.6 V to 0.8 V relative to the Ag/AgCl electrode

(saturated KCl) in the dark. When the frequency is 1 kHz, a Mott-Schottky diagram is constructed, which satisfies the Mott-Schottky hypothesis.

3. RESULTS AND DISCUSSION

3.1 Analysis of structure and morphology

The XRD spectra of the Bi_2MoO_6 thin-film photoelectrode with and without adding the surfactant CTAB are shown in Figure 3. A number of enhanced diffraction peaks could be observed at 2θ=28.24°, 32.59°, 33.07°46.72°, 55.45°, 56.16° and 58.42°, corresponding to the (131), (002), (060), (202), (331), (262) crystal planes, respectively. The positions of the diffraction peaks coincided with the XRD standard card of Bi_2MoO_6 (JCPDS 21-0102), indicating that it was in the orthogonal system crystal phase. Besides, no other peaks for impurity phases were observed, further suggesting that Bi_2MoO_6 was highly pure. After calcination at 400°C for 3 h in a muffle furnace, the sample with adding CTAB (BMO-1) exhibited stronger and sharper diffraction peaks of (131), (002), (060) and (202) crystal planes than the sample without adding CTAB (BMO-0). These results indicated that theBi_2MoO_6 nanosheets in these crystal planes continuously grew because the intensity of the peak is closely related to its morphology. The average grain size of the Bi_2MoO_6 photoelectrode for BMO-0 and BMO-1 was 41.25 nm and 20.41 nm, respectively. The self-assembly of Bi_2MoO_6 was greatly promoted by adding surfactant, thus resulting in its nanosheet structure with smaller crystal grains and better dispersion.
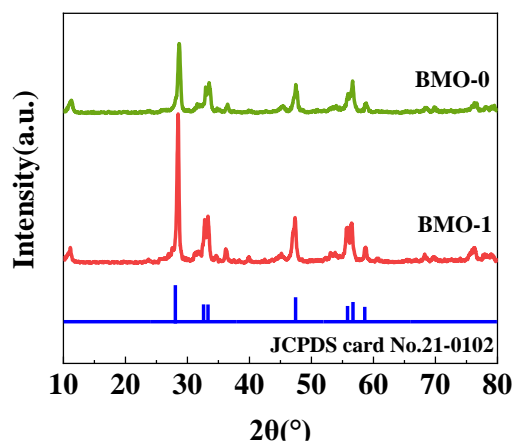

Figure 3. XRD patterns of bismuth molybdate (BMO-0) and CTAB bismuth molybdate (BMO-1) photoelectrodes

The basic morphology and microstructure of BMO-0 and BMO-1 were analyzed by FESEM, as shown in Figure 4. According to Figure 4(a) and Figure 4(b), the surface of the photoelectrode was composed of lamellar structures which were randomly combined and unevenly distributed. Figure 4(c) and Figure 4(d) are FESEM images of the Bi_2MoO_6 photoelectrode with adding the surfactant CTAB. As can be clearly seen from the figures, the agglomeration of Bi_2MoO_6 was significantly reduced by adding the surfactant CTAB, thus forming a nanosheet structure. TF142 and nanosheets grew well and

were evenly distributed, with a diameter of 200 nm to 300 nm and a thickness of 10 nm to 20 nm.
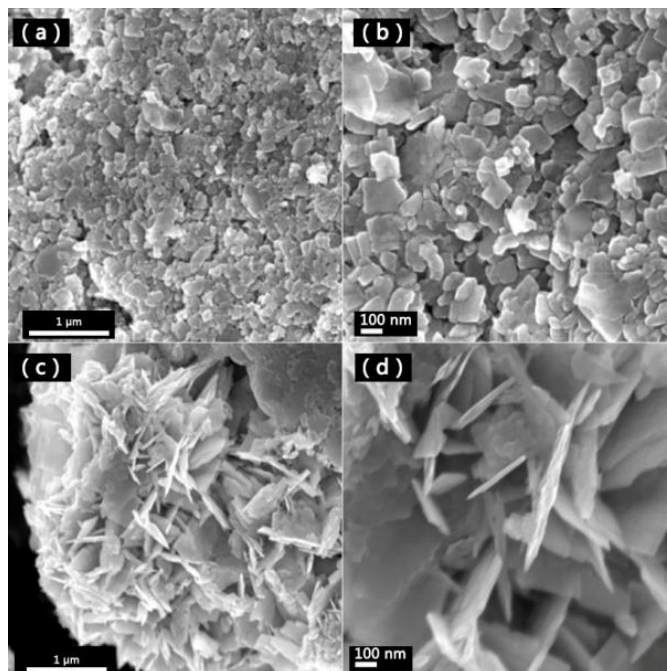

Figure 4. FESEM images of (a) and (b) bismuth molybdate photoelectrode, (c) and (d) bismuth molybdate photoelectrode synthesized in the presence of CTAB

3.2 Spectral analysis

Raman spectroscopy is an effective tool for characterizing material structure. The Raman spectra of the bismuth molybdate containing CTAB (BMO-1) and the surfactant-free bismuth molybdate (BMO-0) stripped from the FTO substrates were shown in Figure 5. A characteristic band of γ-Bi_2MoO_6 was observed . As shown by the Raman spectra of BMO-1 and BMO-0, a strong peak appeared at 799.11 cm^{-1}, accompanied by two peaks at 849.6 cm^{-1} and 715.6 cm^{-1}, corresponding to the Mo-O tensile vibration of the deformed octahedral MoO_6. The peaks at 349.93 cm^{-1}, 283.65 cm^{-1}, 196.64 cm^{-1} and 154.2 cm^{-1} also indicated the vibration of Mo-O bond, which is similar to the reports in the literature[25]. However, some different peaks appeared in the Raman spectra of BMO-1 and BMO-0 because the self-assembly of Bi_2MoO_6 nanosheet structure was affected by adding CTAB. It is consistent with what is shown in the FESEM images where a thinner nanosheet structure was displayed.
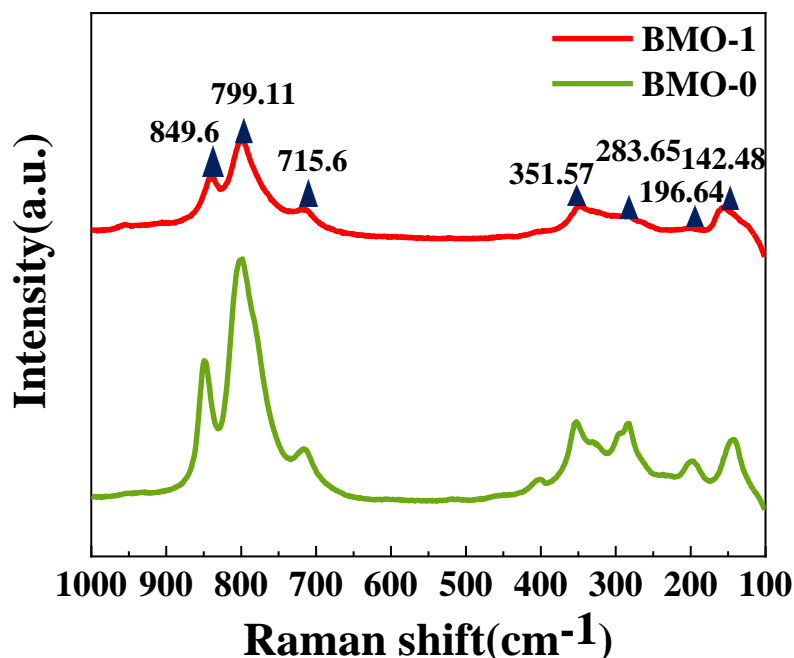
Figure 5. Raman spectra of BMO-1 and BMO-0 stripped from FTO

To determine the optical properties, the UV-Vis DRS spectra of the BMO-1 and BMO-0 photoanodes were obtained, as shown in Figure 6. As can be seen from the figure, the absorption edges of BMO-1 and BMO-0 were 521 nm and 495 nm, respectively. And the UV-Vis DRS spectra of BMO-1 exhibited a significant red shift, indicating that it enhanced the utilization of visible light, which is consistent with other researcher's findings. The energy gap of the sample can be determined by the following formula:

$$\alpha h v = A(h v - E_g)^{n/2} \quad (2)$$

where α is the light absorption coefficient, v is the light frequency, h is a constant, A is a constant, and Eg is the energy band gap.

According to the literature, Bi_2MoO_6 is a direct transitional semiconductor material, and the value of n is 1[26]. Therefore, the band gap energy of BMO-1 and BMO-0 could be estimated based on the relationship between the coefficient of light absorption $(\alpha h v)^2$ and energy $(h v)$. The band gaps of BMO-1 and BMO-0 were 2.23 eV and 2.57 eV (shown in Fig. 6), which are basically consistent with those reported in the literature[27]. In addition, the optical band gap of BMO-1 was narrowed, thus forming a nanosheet structure, which could be attributed to the addition of the surfactant CTAB.
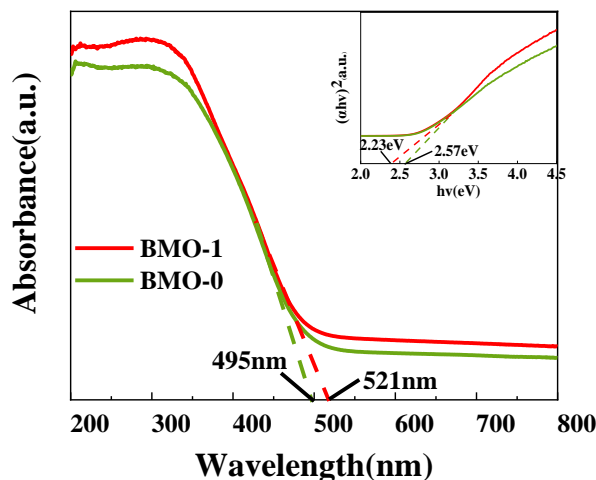
Figure 6. UV-visible diffuse reflection spectra and optical band gap $(\alpha h v)^2$-hv diagrams of BMO-1 and BMO-0

3.3 Analysis of electrochemical impedance

As shown in Figure 7, the Nyquist curve represents the electrochemical impedance spectra of BMO-0 and BMO-1, and its semicircular diameter represents the magnitude of the impedance. According to the figure, the impedance of BMO-1 is smaller than that of BMO-0, indicating that the higher electron mobility can be obtained by a smaller and thinner nanosheet active groups, thereby making it less likely for electrons to recombined with holes, and further confirming that the bias voltage can promote charge transfer to prevent photogenerated electrons from recombining with photogenerated holes[28].
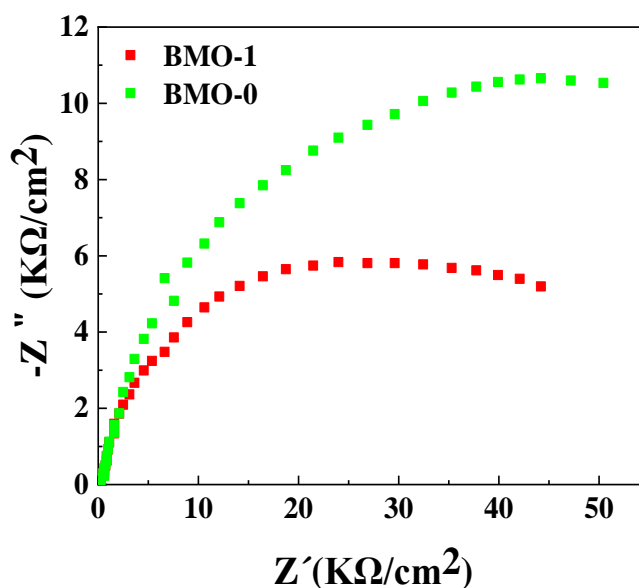

Figure 7. Electrochemical impedance spectra of BMO-1 and BMO-0 (EIS data were measured at a sinusoidal voltage perturbation voltage of 10 mV between 100 kHz and 0.1 Hz)

3.4 Transient photocurrent response spectrum analysis

To further investigate the PEC conversion activity of the prepared photoelectrode, PEC testing was carried out under the visible light (λ>420 nm), and the result is shown in Figure 8. According to the figure, the photocurrent of BMO-0 under visible light was approximately 0.019 μA/cm^2 because the sample without adding the surfactant CTAB exhibited random nanosheet structures. After the sample was added by the surfactant CTAB, its photocurrent was 0.029 μA/cm2, with a significantly improved photocurrent density, which was is mainly because the surfactant enabled Bi_2MoO_6 to self-assemble into a smaller and thinner nanosheet structure, thus increasing active sites and effectively separating photogenerated carriers. Therefore, BMO-1 exhibited a stronger photocurrent response, indicating that its photocatalytic activity was also higher, which are consistent with the experimental results.
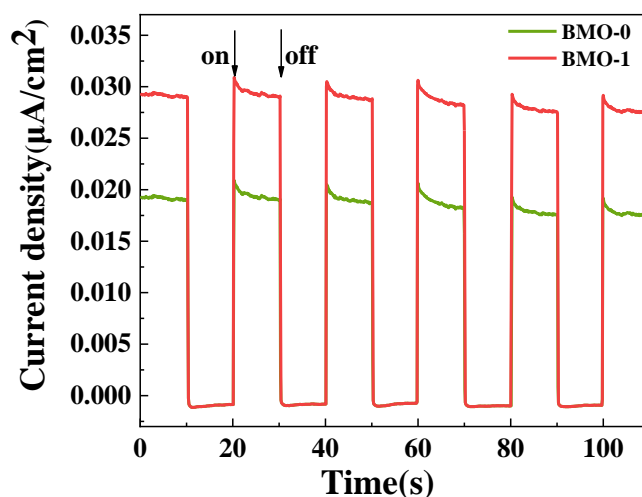
Figure 8. Photocurrent response diagram of BMO-1 and BMO-0
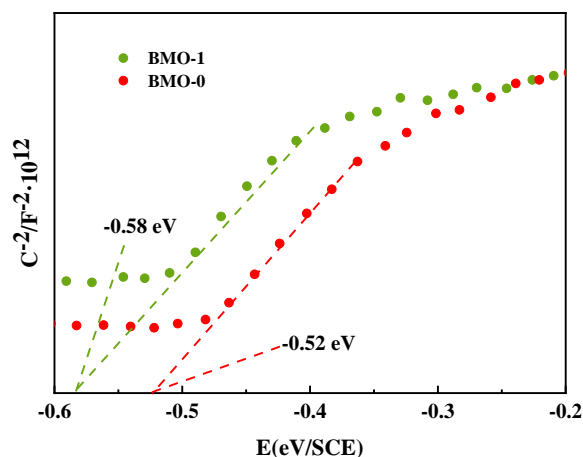
3.5 Mott-Schottky test

Figure 9. Mott-Schottky test chart for BMO-1 and BMO-0

Figure 9 shows a Mott-Schottky test chart of BMO-0 and BMO-1. The intercept of extension line and horizontal axis in the figure indicates the flat band potential, and the slope of the extension line reflects the type of semiconductor. As can be seen from the figure, the slope of the straight line was greater than zero, indicating that both BMO-0 and BMO-1 are n-type semiconductors. Additionally, the flat band potentials of BMO-0 and BMO-1 were -0.52 eV and -0.58 eV, respectively, and the conduction band potentials of BMO-0 and BMO-1 were 2.05 eV and 1.65 eV, respectively, which could be calculated from the previously measured forbidden band width. Furthermore, the different carrier concentrations of different systems will result in a change of the slope of the curve. The carrier concentration (ND) is calculated as follows[29-31]:

$$N_D = \frac{2}{\varepsilon\varepsilon_0 e} \frac{dE}{d\frac{1}{C^2}} = \frac{2}{\varepsilon\varepsilon_0 e} \frac{1}{slope} \quad （3）$$

where N_D is the n-type semiconductor carrier density , ε is the semiconductor's dielectric constant, ε_0 is the vacuum permittivity (vacuum permittivity, $8.85\times10\text{-}14 F\cdot cm\text{-}2$), e is an electron charge, E is an applied voltage, and C is a space charge capacitance. According to the above formula, the carrier density (ND) is known. The lower the slope of the Mott-Schottky curve, the higher its carrier density[32-35]. It can be seen that the carrier concentration BMO-1 is greater than that of BMO-0.

The energy band value can be calculated by above test, as shown in Figure 10. The valence band and conduction band of BMO-0 were 2.05 eV and -0.52 eV, respectively, and the valence band and conduction band of BMO-1 were 1.65 eV and -0.58 eV, respectively. Meanwhile, OH-/·OH=2.38eV, and $O_2/·O_2$-=-0.29eV. Therefore, BMO-0 and BMO-1 can produce superoxide anions and free radicals but not hydroxyl groups.
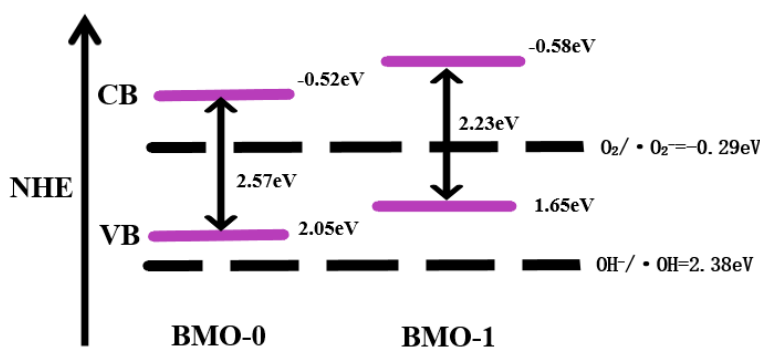

Figure 10. Energy band diagram of BMO-1 and BMO-0

3.6 Visible-light photocatalytic performance of sample in methylene blue solution

The kinetic curves of the methylene blue solution photocatalysis by bismuth molybdate synthesized with (BMO-1) and without adding the surfactant CTAB (BMO-0) are shown in Figure 11. As shown in the figure, the degradation efficiency of BMO-1 and BMO-0 was 87% and 61%, respectively, with a difference of 26%. Table 1 compares this material with several similar
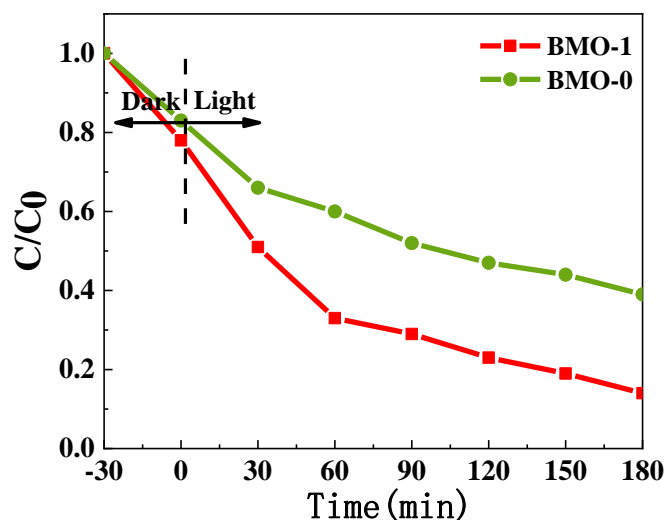
photocatalysts used for MB degradation.

Figure 11. Kinetics of photodegradation of MB under visible light (Use 300W xenon lamp as the visible light source and 10mg/L methylene blue as the degradation target)

Table 1. Degradation effect of different photocatalysts on MB

Catalyst of light	Active substance	Degradation time(min)	MB initial concentration(mg/L)	Degradation efficiency(%)	Reference
CTAB-ZnO	CTAB	180	10	83.6	[36]
Ag_3PO_4/HAP	Ag_3PO_4	180	10	70.39	[37]
Mesoporous TiO_2	CTAB	180	10	74.3	[38]
Bi_2MoO_6	CTAB	180	10	87	this study

4. CONCLUSION

The morphology of the Bi_2MoO_6 photoelectrode plays an importance role on its photoelectrocatalytic properties, and the Bi_2MoO_6 photoelectrode with different morphology can be obtained with or without adding surfacetant (CTAB) by hydrothermal method. The morphology and photoelectrocatalytic properties of the Bi_2MoO_6 photoelectrode obtained with and without adding the surfactant CTAB were investigated in this study. The experimental results are as follows:

(1) The Bi_2MoO_6 with irregular granules was synthesized by hydrothermal method. On this basis, the Bi_2MoO_6 nanosheets were successfully synthesized with surfactant CATB-assisted hydrothermal method, and its morphology was also regulated.

(2) The Bi_2MoO_6 prepared by adding the surfactant CTAB exhibited a wide range of spectral response, high absorbance, excellent ability in separating optimal photogenerated carriers and high

Int. J. Electrochem. Sci., 17 **(2022)** Article Number: 220136

12

transmission efficiency. It is why its photocatalytic activity were enhanced.

(3) The experimental results of MB degradation showed that the the degradation efficiency of nanosheet Bi_2MoO_6 synthesized by adding the surfactant CTAB was increased by 87%, about 1.4 times of that of the Bi_2MoO_6 whose morphology was not regulated, indicating that morphology regulation plays an important role in improving the catalytic performance of Bi_2MoO_6.

References

1. A. Oztürk, M. I. Abdullah, *Total Environ. Sc*i., 358 (2006) 137.
2. M. Zhang, C. Z. Yang, W. H. Pu, Y. B. Tan, K. Yang, J. D. Zhang, *Electrochim. Acta,* 148 (2015) 180.
3. G. Peers, S. A. Quesnel, N. M. Price, *Limnol. Oceanogr.*, 50 (2005) 1149.
4. X. C. Meng, Z. S. Zhang, *Catal. Today*, 315 (2018) 2.
5. L. Yang, C. Wang, Z. Ye, *Rsc Adv.*, 35 (2017) 21686.
6. C. Kongmark, R. Coulter, S Cristol, Cryst. *Growth Des.*, 12 (2012) 5994.
7. W. Zhao, A. J. Wang, Y. Wang, C. C. Lv, W. H. Zhu, S. P. Dou, Q. Wang, Q. Zhong, *J. Alloy. Compd.*, 726 (2017) 164.
8. H. B. Fang,M. X. Xu, L.Ge, *T. Nonferr. Metal. Soc.*, 16 (2006) 373.
9. S. Hu, K. Scheuch, J. G. Gayles, *Rsc Adv.*, 8 (2018) 173.
10. S. X. Oyang, H. T. Zhang, D. F. Li, *J. Phys. Chem. B.*, 110 (2006) 11677.
11. T. Hu, Y. Yang, K. Dai, *Appl. Surf. Sci.*, 31 (2018) 473.
12. N. R. Khalid, E. Ahmed, Z. Hong, *Appl. Surf. Sci.,* 263 (2012) 254.
13. S. R. Kashfi, S. Yazdani, A. Alemi, *Langmuir*, 32 (2016) 10967.
14. P. M. Aiswarya, R. Ganesan, R. Rajamadhavan, T. Gnanasekaran, *J. Alloy. Compd.*, 745 (2018) 744.
15. S. Bdey, N. F. Bourguiba, S. N. Savvin, C. Falah, M. F. Zid, P. Nunez, Synthesis, *J. Alloy. Compd.*, 762 (2018) 806.
16. H. Elhosiny Ali, Yasmin Khairy, *Optik*, 178 (2019) 90.
17. C. Yu , J. C. Yu, C. Fan, *Mater. Sci. Eng. B.*, 166 (2010) 213.
18. M. Vila, C. Díaz-Guerra, J. Piqueras, *J. Alloy. Compd.*, 728 (2017) 827.
19. Y. Y. Li, B. Hui, L. K. Gao, F. F. Li, J. Li, *Colloid Surface A*, 556 (2018) 284.
20. L. Gan, Z. Y. Lu, D. Cao, Z. L. Chen,*Mat. Sci. Eng. C.*, 82 (2018) 41.
21. C. Amirthavalli, J. M. Thomas, K. Nagaraj, A. A. M. Prince, *Mater. Res. Bull.*, 100 (2018) 289.
22. X. R. Han, F. Liao, Y. F. Zhang, Z. Y. Yuan, H. Y. Chen, C. J. Xu, *Mater. Lett.*, 210 (2018) 62.
23. R. Mukkabla, S. Deshagani, M. Deepa, S. M. Shivaprasad, P. Ghosal, *Electrochim. Acta*, 283 (2018) 63.
24. S. I. El-Hout, C. L. Chen, T. Liang, L. F. Yang, J. Zhang, *Mater. Chem. Phys.*, 198 (2017) 99.
25. H. H. Li,K. W. Li, W. Hao, *Chinese J. Inorg. Chem.*, 25 (2009) 512.
26. R. Adhikm, G. Gyawali, S. H. Cho, *J. Solid. State Chem.*, 209 (2014) 74.
27. Y. N. Yang, C. Wang, X. M. Li, *J. Synth. Cryst.*, 7 (2018) 1366.
28. F. M. Pesci , G. Wang , D. R. Klug, *J. Phys. Chem. C.,* 117(2013)25837.

29. W. J. Yin, L. J. Bai, Y. Z. Zhu, *Acs Appl. Mater. Inter.,* 8 (2016) 23133.
30. K.Gelderman, L. Lee, S. W. Donne, *J. Chem. Educ.*, 84 (2007) 685.
31. L. K. Preethi, R. P. Antony, T. Mathews*, Int. J. Hydrogen. Energy*, 41 (2016) 5865.
32. Q. Bi, Y. Gao, C. X. Dang, *CrystEngComm.*, 21 (2019) 6744.
33. Y. Q. Liu, L. Y. Xie, F. B. Meng, X. M. Zhong, F. Q. Dong, M. X. Liu, *Environ. Sci. Technol*., 42 (2019) 58.
34. H. Jin, J. Wang, Y. Ji, M. M. Chen, Y. Zhang, Q. Wang, Y. Q. Cong, *J. Phys. Chem.*, 31 (2015) 955
35. S. Wang, L. Wang, F. Gao, J. K. Cao, M. Liu, *J. China Univ. Min. Technol.*, 42 (2013), 95.
36. Y. Y. Ren, X. Fu, *Shandong Huagong*., 49 (2020) 19.
37. C. Song, L. H. Zhao, M. Y. Qi, R. W. Sun, Q. Zhu, *J. Inorg. Chem.*, 36 (2020) 521.
38. M. M. Bai, D. Yuan, X. K. An, Y. Meng, X. H. Bai, X. G. Ma, *J. Industrial Catalysis*, 28 (2020) 27.